Novel Synthesis of 3D Mesoporous FePO$_4$ from Electroflocculation of Iron Filings as a Precursor of High-Performance LiFePO$_4$/C Cathode for Lithium-Ion Batteries

Jiawu Peng, Xiaoting Hong,* Qiongxiang Zhou, Kwan San Hui, and Bin Chen

Read Online

ACCESS | Metrics & More | Article Recommendations | SI Supporting Information

ABSTRACT: This study presents an economic and environmentally friendly method for the synthesis of microspherical FePO$_4$·2H$_2$O precursors with secondary nanostructures by the electroflocculation of low-cost iron fillers in a hot solution. The morphology and crystalline shape of the precursors were adjusted by gradient co-precipitation of pH conditions. The effect of precursor structure and morphology on the electrochemical performance of the synthesized LiFePO$_4$/C was investigated. Electrochemical analysis showed that the assembly of FePO$_4$·2H$_2$O submicron spherical particles from primary nanoparticles and nanorods resulted in LiFePO$_4$/C exhibiting excellent multiplicity and cycling performance with first discharge capacities at 0.2C, 1C, 5C, and 10C of 162.8, 134.7, 85.5, and 47.7 mAh·g^{-1}, respectively, and the capacity of LiFePO$_4$/C was maintained at 85.5% after 300 cycles at 1C. The significant improvement in the electrochemical performance of LiFePO$_4$/C was attributed to the enhanced Li$^+$ diffusion rate and the crystallinity of LiFePO$_4$/C. Thus, this work shows a new three-dimensional mesoporous FePO$_4$ synthesized from the iron flake electroflocculation as a precursor for high-performance LiFePO$_4$/C cathodes for lithium-ion batteries.
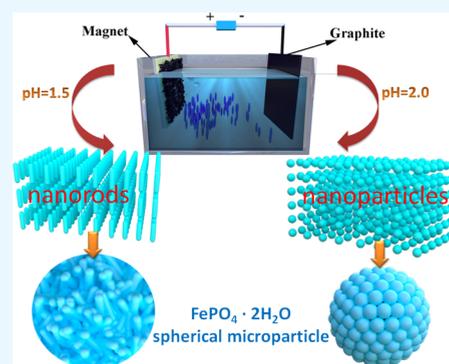
1. INTRODUCTION

In recent years, with the ever-growing demand for portable electronic and environmentally friendly devices due to the energy crisis and environmental pollution, the development of efficient and robust electrochemical energy storage or conversion systems is imminent.[1] There is widespread popular support for using lithium-ion batteries (LIBs), which provide electricity without giving rise to any carbon dioxide emissions.[2]

Among many potential cathode materials, the LiFePO$_4$ (LFP) cathode has attracted great attention since its discovery in 1997.[3] The LiFePO$_4$ battery chemistry offers numerous clear advantages such as environmentally friendly, non-combustibility, high thermal stability, good cycle stability, and a flat discharge potential at 3.4 V vs Li/Li$^+$. However, LFP's low electric conductivity ($\sim10^{-11}$ cm^2 S^{-1}) and low Li-ion diffusion kinetics ($0-1.8 \times 10^{-4}$ cm^2 S^{-1}) at room temperature, which becomes even weaker at lower temperatures, limit its application in fields that require high rate capability.[4,5] To overcome these problems, many specific modifications based on the structure−performance relationship have been tried to improve the rate performance of LFP, such as specific controls of particle size,[6,7] shape, and morphology.[8−10]

Lithium-ion diffusion in LFP is preferably one-dimensional along the *b*-axis.[11,12] It is evident that the nanostructure facilitates shorter ion diffusion paths, resulting in high efficiency.[13,14] Various methods have been developed to prepare nanostructure LFP particles to facilitate Li$^+$ diffusion, including hydrothermal/solvothermal,[15,16] sol−gel,[17] and hard-templating approaches.[18−20] Surface conductive coating and ion doping are complementarily used to enhance the migration of electrons.[21−23] However, the high-performance nano-structured LFP suffers from low tap density and volumetric energy density limitations.[24] With these drawbacks, extensive studies have been initiated to explore novel LFP nanostructures. By combining the advantages of nanoscaled building bricks and microscaled assemblies.[25] The novel hybrid with self-assembled nano/microstructures is highly pursued to improve the self-assembling nanoscale building blocks and is becoming an intensive and popular research topic.[26,27]

Many research efforts have been focused on the development of various LFP synthetic techniques and products with multifarious self-assembled morphologies and carbon-coated LFP cathode materials. In this regard, Goodenough et al. first reported the three-dimensional (3D) LFP architectures by a modified solvothermal approach combined with high-temperature calcination.[28] These flower-like LiFePO$_4$ microspheres

consist of many nanoplates interweaved together with open 3D porous microstructures, which has been proved to facilitate electrolyte penetration into the electrode particles. A porous and coarse LiFePO$_4$/C nanocomposite was also obtained by a simple and novel growth technique using LFP nanocrystals as a seed crystal and presented a high initial discharge capacity of 155 mAh g^{-1} at 0.1C.[29] The micro/nanostructure LFPs with various morphologies ranging from cube cluster to rugby-like structure were synthesized using poly(ethylene glycol) via controlling the pH values of the precursor solutions and exhibited a great high-rate capacity of 152 mAh g^{-1} at 0.1C.[30] The structure and morphology of the LiFePO$_4$/C cathode material were also investigated using a divalent precursor of Fe$_3$(PO$_4$)$_2$·8H$_2$O as the iron source in a polyol process and subsequent surface modification via co-precipitation process with variable reaction time. LiFePO$_4$/C showed an excellent rate capability (153 mAh g^{-1} at 1C) and cycle performance (the capacity retention of 97% after 300 cycles at 10C).[30] The above-mentioned carbon coating can be carried out ex situ or in situ. Basically, any organic compound with a high degree of sp^2-hybridized carbon atoms can be considered to improve the electron migration of FePO$_4$, as long as it can be transformed into a carbon shell with a suitable degree of graphitization.

Additionally, it has been widely accepted that the electrochemical performance of LiFePO$_4$/C is closely related to the FePO$_4$ precursor involving the influence of particle agglomeration, morphology, crystallinity, etc.[31−33] A large number of amorphous or crystalline iron phosphates have been synthesized in recent years using different co-precipitation routes.[34,35] Numerous nanostructures including hydro-micro ball, fusiform, shuttle-shaped particles, and uniform core−shell structures were synthesized by adjusting various parameters such as solution pH, reaction and aging temperature, and concentration and type of reactants.[36,37] However, subsequent water treatment is inevitably required for the reaction residue in the co-precipitation process. Therefore, the development of a cheap, efficient, and environmentally friendly FePO$_4$ is a promising utilization route for the innovation of the synthetic method.

To the best of our knowledge, there are no reports about 3D FePO$_4$ architectures consisting of nanorods or nanosphere particles assembled into a total particle size in the micron range. This purpose was achieved by a novel economical and environmentally benign way to synthesize FePO$_4$ by iron filings electrolytic anodic flocculation coupled with the solvent heat treatment. It is a novel sustainable FePO$_4$ preparation method from iron filings waste with the advantages of no discharge and recyclability of the bath liquid. This study further presents an interesting approach to controlling the morphology of the microspheres by tuning the complex chemical processes of crystal nucleation and growth. Subsequently synthesized LiFePO$_4$/C exhibits high discharge capacity and low electrode charge-transfer resistance for lithium-ion batteries after being routinely coated by glucose carbon based on the above FePO$_4$ precursor.

2. EXPERIMENTAL SECTION

2.1. Material Preparation. *2.1.1. Preparation of FePO$_4$.* The FePO$_4$ precursor was prepared through the electrolytic anode flocculation method on iron fillings waste (Henan Longxin Materials Co., Ltd.) in a two-electrode system with a simple DC power supply. A graphite plate (Shenzhen Tailin Graphite Co., Ltd.) and a titanium plate (Hebei Hongyun

Metal Materials Co., Ltd.) with the same size of 20 cm × 16 cm × 0.2 cm are used as the cathode and the anode with a constant distance of 4 cm, respectively. A certain amount of iron fillings was evenly distributed on the titanium plate and fixed by a magnet plate (18 cm × 14 cm × 0.2 cm) outside of the reaction tank. The reaction medium (30 mL) was aqueous solvent continuously adjusted by a mixture of H$_3$PO$_4$ (AR, 85%) and H$_2$O$_2$ (AR, 30%) (1: 1) to pH of 1.0, 1.5, 2.0, and 2.5. Milky white precipitates (hydrated ferric phosphate) were obtained at a current density of 11.4 mA cm^{-2} and a temperature of 90 °C for 30 min. Finally, the precipitates were collected by filtration, washed several times with distilled water, and finally dried in a vacuum oven at 80 °C for 12 h. Two samples from different pH values (1.5, 2.0, 1.0, and 2.5) of the reaction solution were named FP-I, FP-II, FP-III, and FP-IV, respectively.

2.1.2. Preparation of LiFePO$_4$/C. The LiFePO$_4$/C composite samples were synthesized using Li$_2$CO$_3$ (AR, 99.5%) as the lithium source for the FePO$_4$ precursor with a Li/Fe molar ratio of 1.02 and C$_6$H$_{12}$O$_6$ (AR, 10%) as the carbon source. After being well mixed, the slurry was dried in a vacuum drying oven at 80 °C for 12 h and then transferred to a tube furnace by calcination at 750 °C for 10 h using a reducing gas atmosphere. The obtained LiFePO$_4$/C using precursors I, II, III, and IV were defined as LiFePO$_4$/C-I, LiFePO$_4$/C-II, LiFePO$_4$/C-III, and LiFePO$_4$/C-IV, respectively.

2.2. Characterization. The phase purity and crystalline structure of the samples were determined by X-ray diffraction using Cu Kα radiation (XRD, D/max 2200/PC, Rigaku, 40 kV, 20 mA, 1.5406 Å) in an angular range (2θ) from 10 to 80°. The thermal stability of hydrous FePO$_4$ was studied using a Mettle Toledo thermogravimetric/differential scanning calorimetry (TG/DSC) under an N$_2$ atmosphere at a heating rate of 10 °C/min. The specific surface area and pore size distribution were obtained via a high-performance automatic mercury porosimeter (Micromeritics. Auto pore IV 9500). The morphology and microstructure of the samples were observed using scanning electron microscopy (SEM) (Sigma-300) and high-resolution transmission electron microscopy (HRTEM, JEOL JEM200PLUS), respectively. Particle size was averaged by more than 210 particles from SEM images. Fourier transform infrared spectroscopy (FT-IR) spectra were measured on a Thermos IS10 FT-IR spectrometer. The chemical composition of the precursors was analyzed by X-ray photoelectron spectroscopy (XPS, Thermo Fisher ESCALAB 250Xi).

2.3. Electrochemical Measurement. The electrochemical performances were evaluated by a 2016-coin-type button cell assembled with the cathode electrode, a metal lithium foil as both reference and anode electrodes, polypropylene film (Celgard 2400) as a separator, and a solution of 1 M LiPF$_6$ in ethylene carbonate and dimethyl carbonates (1:1 in volume) as the electrolyte. The cell assembly and sealing were carried out in an argon-filled glovebox under an atmosphere with concentrations of moisture and oxygen below 1 ppm. For the preparation of the cathode electrode, the active materials (LiFePO$_4$/C-I and LiFePO$_4$/C-II, loading amount of 1−1.2 mg cm^{-2}), acetylene black, and poly(vinylidene fluoride) (PVDF) binder were uniformly mixed with a weight ratio of 80:10:10 using N-methyl-2-pyrrolidinone (NMP) solvent. The mixtures were coated on an aluminum foil with a thickness of 0.025 µm and then dried in a vacuum oven at 120 °C for 10 h before cell assembly. The galvanostatic charge and discharge
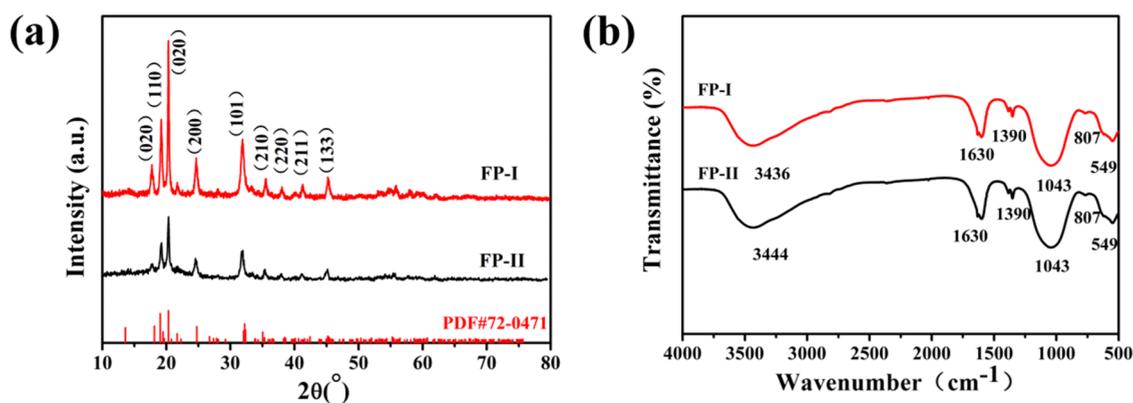
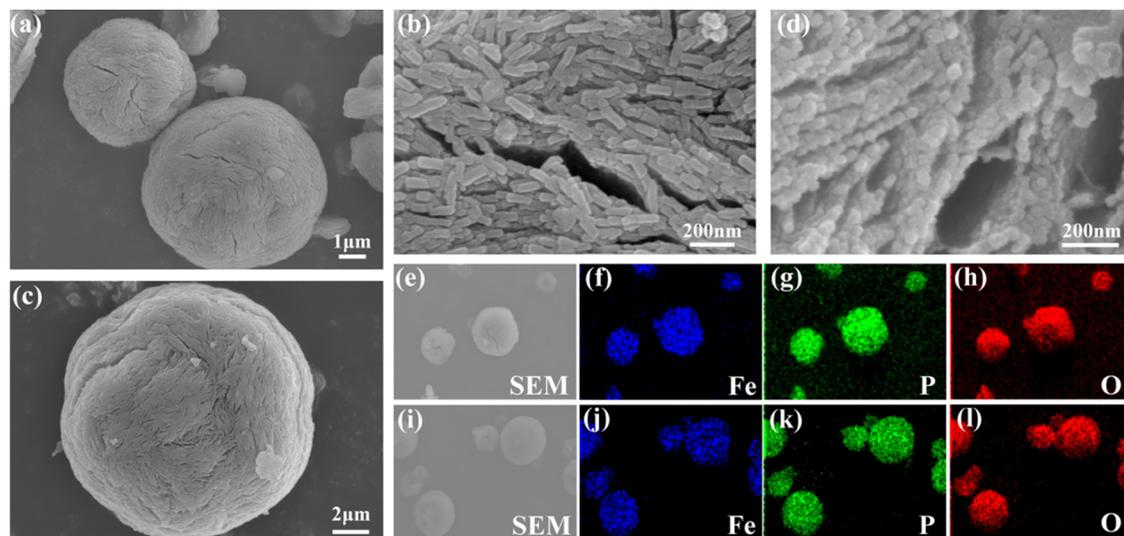**Figure 1.** XRD patterns (a) and FT-IR spectra (b) of FePO$_4$·2H$_2$O precursors.

Figure 2. SEM images of FePO$_4$·2H$_2$O precursors I (a, b) and II (c, d). Elemental mapping of FePO$_4$·2H$_2$O precursors I (e–h) and II (i–l).

tests were performed in a voltage window between 2.3 and 4.2 V at 25 °C on a multichannel battery testing system (LAND CT2001A). Electrochemical impedance spectroscopy (EIS) measurements were carried out in two-electrode cells on a CHI660E electrochemical workstation, using a ±5 mV AC signal amplitude and frequency range from 0.1 to 100 HZ. The cycling voltammetry (CV) results were obtained in the range of 2.3−4.2 V on the same station.

3. RESULTS AND DISCUSSION

Figure 1a shows the XRD patterns of hydrated ferric phosphate precursors obtained at different reaction solutions of pH 1.5 and 2.0. The XRD patterns of precursors I and II show obvious signals of crystalline characteristics and all diffraction peaks demonstrate a monoclinic structure with a space group P_{21}/n (JCPDS card No. 72-0471). The patterns also reveal a clear increase in the intensity of (110) to (002) planes with the decreasing solution pH during electrolytic anodic flocculation of iron fillings. Figure S1a XRD shows that the precursors prepared from solutions at different reaction pH values of 1.0 and 2.5 are amorphous.

The FT-IR spectra display the characteristic vibrations of PO stretching, water hydroxyl stretching, and water HOH bending in hydrated ferric phosphate (Figure 1b). Two bands around 3469 and 3269 cm^{-1} were observed for the water OH

stretching vibration, indicating the role of hydrogen bonding to bind the neighboring primary nanoparticles together.[38−40] The water HOH bending mode region ($\nu 2$ symmetric bending mode) occurs near 1630 cm^{-1}, indicating both coordination water and chemically bonded water. The band at 807 cm^{-1} is ascribed to the liberational mode vibration of the strongly hydrogen-bonded water molecules. Furthermore, a band near 1043 cm^{-1} is assigned to the antisymmetric stretching vibration of PO and other frequencies observed below 1000 cm^{-1} are assigned to the $\nu 1$ and $\nu 4$ modes of the PO$_4$ group. Thus, FT-IR analysis reveals the molecular structure of hydrated ferric phosphate particles and proves the potential function of the hydrogen bond for a three-dimensional framework assembled from one-dimensional nanoparticles or nanorods.[41]

Figure S3 shows the TG−DSC curves of FP-I and FP-II hydrate precursors. These two TG curves basically showed the same trend. The weight loss occurred primarily below 190 °C and terminated at about 380 °C. The total weight loss is found to be 22.5 and 21.59%, respectively, which remains essentially the same after 380 °C. The weight loss was due to the removal of crystal water from the precursors, indicating that both samples were dehydrated iron phosphate and the weight loss was consistent with the stoichiometric ratio of FePO$_4$ and H$_2$O of 1:2, which is in accordance with the observation elsewhere.[9,42−45] This conclusion can be strengthened by the

DSC curves of the samples. Two exothermic peaks imply that FP-I and FP-II lost two molecules of water at 182.2 and 141.9 °C, respectively. Two endothermic peaks at 547.45 and 553.64 °C just mean that precursors underwent a crystal structure transformation.

The SEM images of two kinds of $FePO_4 \cdot 2H_2O$ precursors are depicted in Figure 2a−d. Elemental mapping images show that two $FePO_4 \cdot 2H_2O$ precursors contain Fe, O, and P elements, which are evenly distributed on the particles (Figure 2e−l). Both precursor I and II show a microspherical secondary structure (Figure 2a,c) with certain nanosized surface cracks, in which precursor I (d_{50} = 3.92 μm, Figure S4) is self-assembled from a considerable number of overlapped nanorods (Figure 2b), while precursor II (d_{50} = 5.69 μm, Figure S4) is composed of numerous interlinked nanoparticles (Figure 2d). As illustrated in Figure S5, $FePO_4 \cdot 2H_2O$ has two-dimensional layer characteristics through an infinite one-dimensional sawtooth chain structure along the b-axis by bridging the (FeO_6) octahedral group with a (PO_4) tetrahedral group in an angle-sharing manner. The three-dimensional structure is formed by complex physical cross-linking of hydrogen bonding.[38,46] The continuous nano-particles and nanorods act as nuclei in the $FePO_4 \cdot 2H_2O$ precipitate. As the reaction proceeds, neighboring nuclei have enough time to come together at planar interfaces, forming an infinite layer parallel to the ac surface. However, unlike I and II, precursors III and IV show a mutually superimposed structure during their formation, supporting the information in S2. At solution pH equal to 1.0 and 2.5, the nuclei become more interconnected and grow along the b-axis of $FePO_4 \cdot 2H_2O$.[47]

$FePO_4 \cdot 2H_2O$ has an experimental value of 3.04 and a theoretical value of 2.95 for the zero charge point. At the beginning of anodic iron fillings electrodissolution, the surface of $FePO_4$ nanoparticles contains both positive $>FeOH^{2+}$ sites and negative $>PO^-$ sites.[48] The smaller the solution pH is, the greater the net charge of $FePO_4$ nanoparticles and the stronger the electrostatic interaction between the two sites.[49] Therefore, at lower particle volume fractions at pH 1.0, nanoparticles form nanospheres with rapid aggregation of the reaction. During the aggregation of particles at pH 1.5 and 2.0, short nanorods and nanoparticles are formed through positive and negative end connections. During aging at large volume fraction, a more complex 3D interconnected "particle network" structure is formed by the electrostatic interactions (including hydrogen bonds). The decrease in the solution solubility at pH 2.5 weakens the electrostatic interactions between the two sites and forms nanospheres with a mesoporous structure.

XPS is employed to characterize the composition and the oxidation state of iron in each precursor. The full survey XPS spectra confirm the presence of Fe 2p, Fe 3s, Fe 3p, O 1s, O 2s, P 2s, and P 2p (Figure S6a), corresponding to molecular components of $FePO_4$.[50,51] Deconvoluted XPS spectra of Fe 2p in Figure S6b,c show peaks at 710.8 and 723.8 eV attributed to the presence of Fe^{2+} and peaks at 713.5 and 727.4 eV related to Fe^{3+}, which is the result of oxidation after the addition of H_2O_2. The contents of ferrous species are observed to decrease from 30.5 to 20.3% with the increasing solution pH. Thus, as confirmed by various characterizations, the crystal structure and morphology of the precursor can be successfully controlled by varying the solution pH.

The XRD patterns in Figure 3 reveal that all $LiFePO_4/C$ products synthesized by the carbothermal reduction were
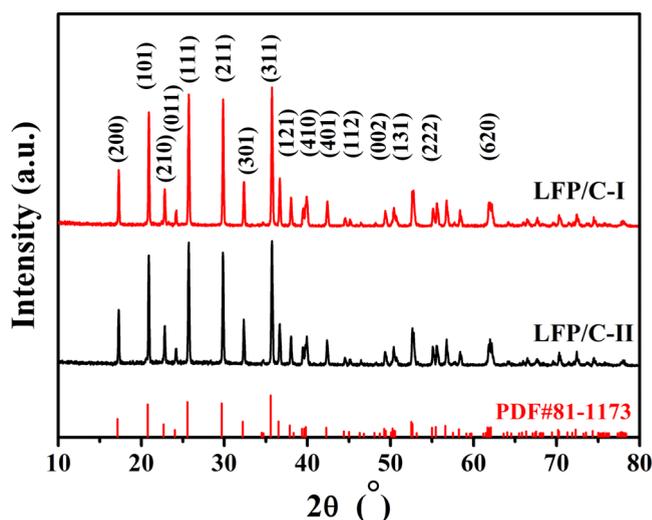

Figure 3. XRD patterns of LFP/C-I and LFP/C-II.

identified as a single phase of $LiFePO_4$ with an ordered olivine structure, indexed to the orthorhombic $Pnma$ group (JCPDS. Card No. 81-1173). Figure S1b indexed to the orthorhombic $Pnma$ group (JCPDS. Card No. 80-2092). Carbon could not be found in the XRD profiles, reflecting that the coated carbon layer was amorphous with negligible influence on the $LiFePO_4$ structure. The Rietveld refinement of the XRD data was applied to extract unit cell parameters (Figure S5 and Table S1). Obviously, the lattice parameters of all LFP samples were indexed to the representative olivine structure with a $Pnma$ space group (orthorhombic crystal structure) in accordance with olivine $LiFePO_4$ (Card No. 81-1173, a = 1.033 nm, b = 0.601 nm, c = 0.469 nm).

Clearly, nanosized primary particles (40−200 nm) that form solid spheres of 1−5 μm as second particles promote highly crystallized olivine place.[52,53]

SEM images show that carbon-coated $LiFePO_4$ samples are of a relatively smooth and 3D near-spherical structure (Figure 4a,b), with an average particle size of <3 μm due to structure collapse during the generation of $LiFePO_4$ from microspherical $FePO_4$ particles. TEM images clearly show carbon-encapsu-lated LFP particles covered by an amorphous carbon layer with a uniform thickness of 2−3 nm (Figure 4c−f). HRTEM images (Figure 4e,f) show that the d-spacing values of the adjacent lattice are 0.302 and 0.431 nm, corresponding to the (211) and (101) planes of the crystal phase LFP with an amorphous carbon shell. Energy dispersive X-ray spectroscopy of LFP confirms the uniform distribution of particles in LFP (Figure 4g−j). Figure S2a,b shows the SEM images of mesoporous and spherical FP precursors, respectively, and Figure S2c,d shows the SEM images of LFP, with element mapping images showing that LFP has a uniform distribution of C, O, Fe, and P (Figure S2e−n) on the particles. The thin carbon layer not only facilitates electron migration for the reverse Fe^{3+} to Fe^{2+} reaction by increasing the electron conductivity but also effectively inhibits the particle growth of $LiFePO_4$, thus improving the morphology and structure of the $LiFePO_4$ core. As the insertion and delamination of electrochemical lithium are usually limited by the diffusion rate, the structure of the cathode material is an important factor in determining the electrochemical performance, with structural changes facilitat-ing adequate contact between the electrode and the electrolyte.
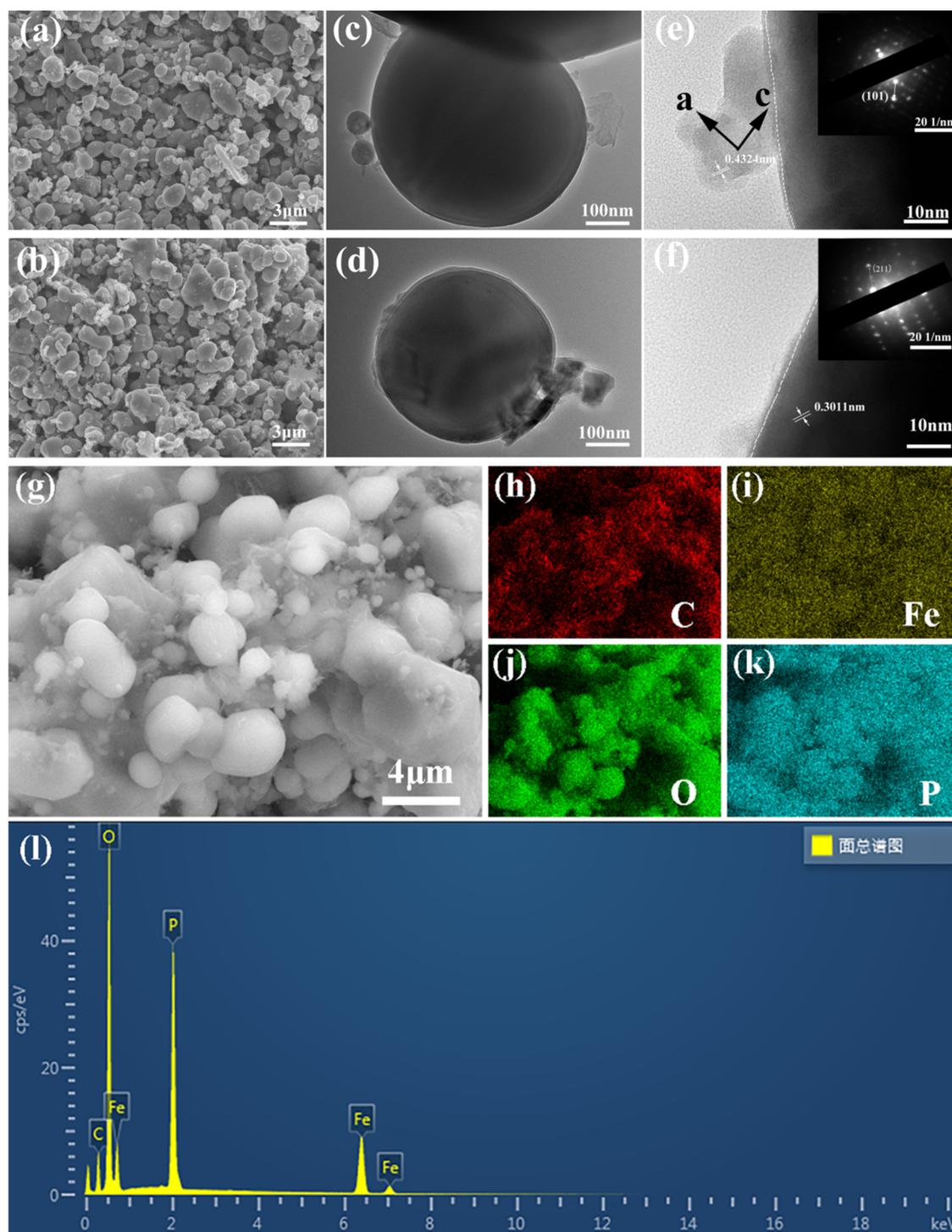
Figure 4. SEM (a, b) and HRTEM images (c−f) of LiFePO$_4$/C synthesized by the carbon thermal reduction process. (g−k) Selected area electron diffraction patterns and (l) EDS energy spectrum of LFP/C.

The vibronic density of the electrode material is directly related to the volumetric energy density of the battery, which can reach approximately 1.211 g·cm^{-3} for LFP-I and 1.240 g·cm^{-3} for LFP-II. This property allows for a higher volumetric energy density of the carbon-coated lithium iron phosphate cathode material.[54,55]

Figure 5a shows the initial charge/discharge profiles of the LFP/C-I and LFP/C- II composites in the range of 2.3 to 4.2 V at a 0.2C (0.034 A g^{-1}) rate. Two samples exhibit a typical flat voltage plateau between 3.5 and 3.4 V (vs Li$^+$/Li), caused

by the Fe^{2+}/Fe^{3+} redox couple during the lithium-ion extraction and insertion process. The initial charge plateau is slightly broader than the discharge one for two samples, which results from slightly overused lithium salt in the carbothermal reduction process, and then more lithium ions are extracted from the LFP/C crystal structure during the first charge.[56] LFP/C-I delivers a higher discharge capacity of 162 mAh g^{-1} compared to 144 mAh g^{-1} for LFP/C-II. Additionally, the voltage difference between the charge/discharge plateau of LFP/C-I (45 mV) is smaller than that of the LFP/C-II
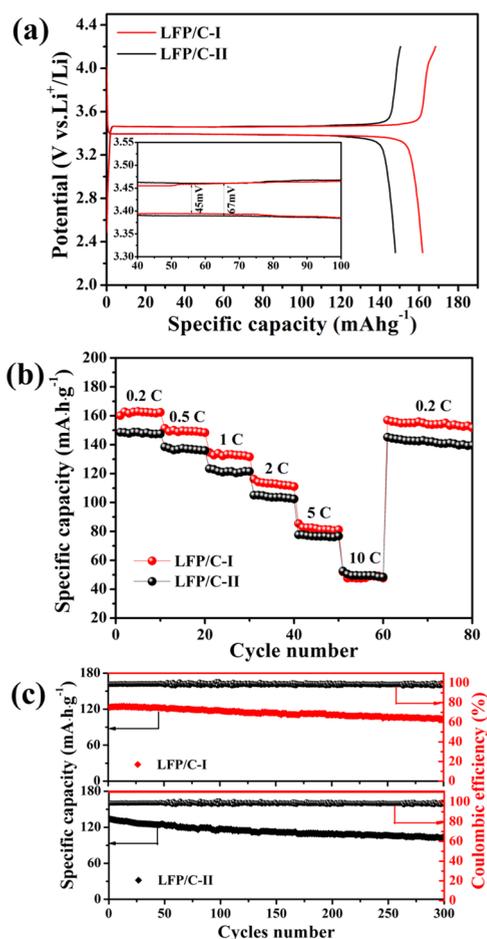
Figure 5. Electrochemical properties of LFP/C-I and LFP/C-II. (a) Galvanostatic charge and discharge profiles at 0.2C. (b) Rate performance at current densities from 0.2 to 10.0C. (c) Cycling performance and Coulombic efficiency at 1C in 300 cycles.

is favorable for diffusion Faradic reaction with fast ion transportation and further improves the rate performance of LFP/C.[59] Higher crystallinity and homogeneous carbon coating in LFP/C-I are also conducive to electrolyte immersion and lithium-ion and electron transfer. For comparison, the electrochemical properties of LiFePO$_4$ synthesized by different methods are listed in Table S2. This confirms the good electrochemical properties of LiFePO$_4$ synthesized in this work and shows a promising alternative approach to preparing the LiFePO$_4$ material.

CV scans were implemented to further study their electrochemical properties to explore more information on the enhanced electrochemical performance of LFP/C-I and LFP/C-II (Figure 6). Figure 6a shows the CV curves at a scan
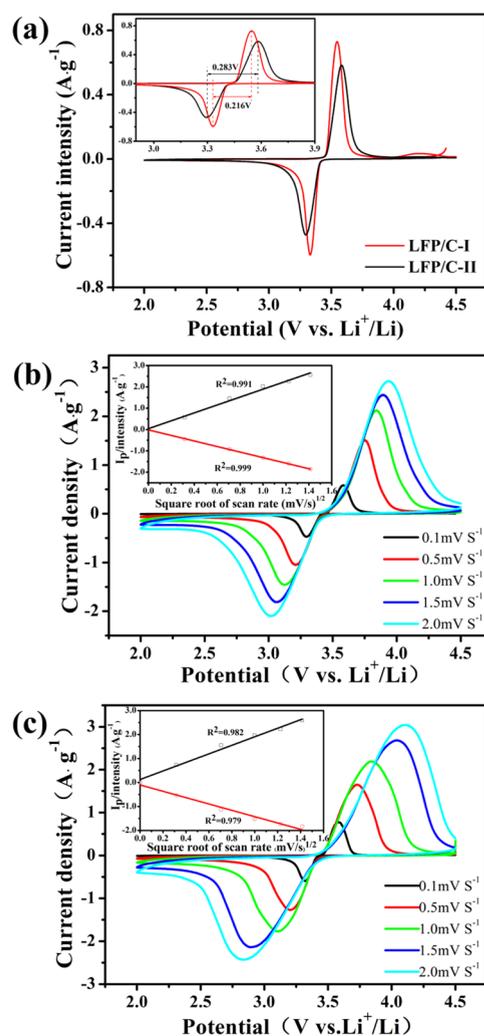

Figure 6. (a) CV curves of LFP/C-I and LFP/C-II at a scan rate of 0.1 mV s^{-1}. CV curves of LFP/C-I (b) and LFP/C-II (c) at different scan rates. The insets are the corresponding plots of I_p and $v^{1/2}$.

electrode (67 mV) indicating superior electrochemical kinetics for LFP/C-I.[57] This should be attributed to the fast reaction and lithium-ion diffusion kinetics of the submicron secondary particles in the single orthorhombic phase consisting of more homogeneous primary nanoparticles.

The discharge curves at various rates (0.2C to 10.0C) revealed the superb rate capabilities of the LFP/C-I electrode, as shown in Figure 5b. As the discharge current density increases from 0.2C to 10.0C, rate capacities accordingly decrease from 162.8 to 85.5 mAh g^{-1}. This normal and frequent phenomenon is a result of the increase of the internal resistance at a high C rate at unreachable thermodynamic equilibrium and is found elsewhere.[58] The LFP/C-I electrode exhibits a better rate performance, and the higher capacities of 162.8, 151.4, 134.7, 116.2, 85.5, and 47.7 mAh g^{-1} were obtained at 0.2, 0.5, 1.0, 2.0, 5.0, and 10.0C, respectively.

The cycling performance of LFP/C-I and LFP/C-II was measured at 1C for 300 cycles, as shown in Figure 5c. The LFP/C-I and LFP/C-II electrodes displayed capacities of 104.1 and 99 mAh g^{-1} coupled with Coulombic efficiencies of 85.5 and 84.7% after 300 cycles, respectively, which indicates a stable cyclic performance. The satisfactory electrochemical and cyclic performance could be first attributed to the 3D mesoporous structure. LFP/C-I has a larger mesopore (Figure S8) and a smaller particle size (shown in BET images), which

rate of 0.1 mV s^{-1} over a potential range of 2.3−4.5 V (vs Li$^+$/Li), where sharp and symmetric anodic/cathodic peaks imply the two-phase charge/discharge reaction of LiFePO$_4$ and FePO$_4$. LFP/C-I shows a higher peak current intensity and a smaller potential difference (216 mV) between the charging and discharging peaks, indicating improved electrode kinetics and reversibility. Figure 6b,c shows the variation trend of CV curves at different scan rates from 0.1 to 2.0 mV s^{-1}. The

potential separation between the oxidation and reduction peaks increases with the scan rate manifesting enhanced polarization at higher charge/discharge current densities. It was found that the peak current densities were proportional to the square root of the scan rate, signifying a reversible oxidation/reduction reaction. The Randles−Sevcik equation describes the relationship between I_p/mass and v as follows

$$I_p = 2.69 \times 10^5 n^{3/2} A D^{1/2} v^{1/2} C \quad (1)$$

where n is the number of electrons transferred per molecule (here $n = 1$), A is the active surface area per unit mass of the electrode ($cm^2\ g^{-1}$), and C is the initial concentration of lithium ions in the LFP crystal ($mol\ cm^{-3}$), which is deemed to be the same for LFP/C-I and LFP/C-II, and D is the Li$^+$ diffusion coefficient ($cm^2\ s^{-1}$).

Based on the above equation, it can be concluded that the electrochemical reaction on the cathode is more efficient as the slope of the plot of I_p and $v^{1/2}$ is larger. The insets in Figure 6b,c shows that the LFP/C-I cathode has a larger slope of 4.0 than that of the LFP/C-I cathode (3.3), which is consistent with the higher rate performance of LFP/C-I in Figure 4b.

To gain an intuitive understanding of the lithium-ion transport kinetics and the involved resistances, EIS is used to further determine the electrode impedance of LFP/C-I and LFP/C-II. As shown in Figure 7, the semicircle in the high-
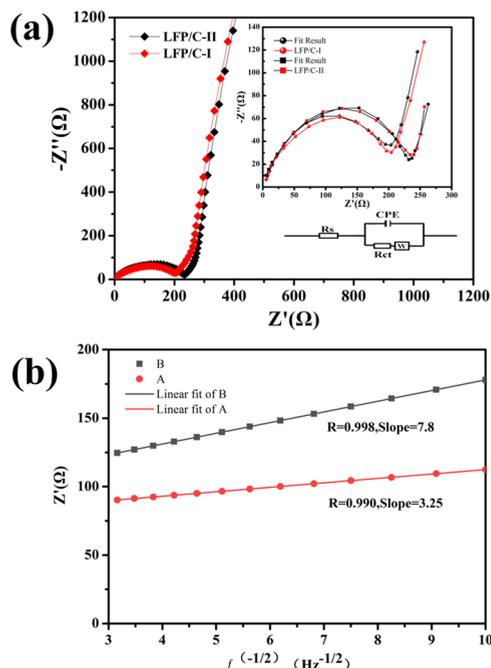

Figure 7. (a) Nyquist plots. The inset is the applied equivalent circuit. (b) Plots of Z' and $f^{(-1/2)}$.

frequency region represents charge-transfer resistance. The straight line in the low-frequency region is ascribed to the diffusion of the lithium ions into the bulk of electrode material. The equivalent circuit model in Figure 7a includes uncompensated resistance (R_e), charge-transfer resistance (R_{ct}), double layer and passivation film capacitance (CPE), and Warburg impedance (Z_w). The fitting values from this equivalent circuit are presented in Table S3. It shows a much smaller depressed semicircle of LFP/C-I electrodes compared to LFP/C-II. Thus, the charge-transfer resistance of LFP/C-I

may be much smaller than that of the LFP/C-II composite, resulting in a higher electronic conductivity of LFP/C-I. In addition, the lithium-ion diffusion coefficient can be calculated according to the following equation

$$D = R^2 T^2 / (2A^2 n^4 F^4 C^2 \sigma_\omega^2) \quad (2)$$

where R is the gas constant; T is the absolute temperature (298 K); F is the Faraday constant; A, n, and C are given in eq 1; and σ_ω is the real Warburg impedance coefficient ($Hz^{1/2}$) related to the real part of impedance Z'. In the low-frequency range, Z' can be written as

$$Z' = R_s + R_{ct} + (2\pi)^{-1/2} \sigma_\omega f^{(-1/2)} \quad (3)$$

where f is the frequency and R is the ohmic resistance. Thus σ_ω can be calculated from a plot of Z' and $f^{(-1/2)}$. Figure 6b shows that the slope of LFP/C-II is 2.4 times greater than that of LFP/C-I. Therefore, the $AD^{1/2}$ of LFP/C-I is 2.4 times that of LFP-II. The lithium-ion diffusion coefficients for I and II are a and b, respectively. Clearly, LFP/C-I has a smaller R_{ct} and a high lithium-ion diffusion coefficient D_{Li}^+. Therefore, it can be illustrated that LFP/C-I exhibits higher electrochemical activity.

4. CONCLUSIONS

In this work, micron-sized spherical $FePO_4$ particles were synthesized by the iron fillings electrolytic anodic flocculation method, which is simple, economical, highly productive, and green and does not require any surfactants or templates. We have demonstrated the variation of the precursor particle size and shape by modulating the pH of the solution. The high electrochemical capacities of the as-synthesized $LiFePO_4$/C composites were 162.8, 134.7, 116.2, 85.5, and 47.7 $mAh\cdot g^{-1}$ at discharge rates of 0.2, 1, 2, 5, and 10C, respectively. The excellent capacity retention after 300 cycles was attributed to the high performance of secondary microspherical particles with primary nanostructure and high exposure to large ac crystal surfaces of the particle surfaces for lithium diffusions.

■ ASSOCIATED CONTENT

Ⓢ Supporting Information

The Supporting Information is available free of charge at https://pubs.acs.org/doi/10.1021/acsomega.2c07838.

XRD patterns of amorphous crystals of the precursor $FePO_4\cdot 2H_2O$ prepared at pH 1.0 and 2.5; SEM images of the observed precursor morphology and EDS analysis of the corresponding element mapping; XRD mapping by carbon thermal reduction to $LiFePO_4$/C and SEM analysis; TG−DSC curves of FP-I and FP-II sample precursors recorded at temperatures ranging from 25 to 800 °C; particle size distribution of the synthesized precursors at different gradients of pH; XPS spectral analysis; Brunauer−Emmett−Teller (BET) and pore size distribution; schematic diagrams of the monoclinic crystal structure and synthesized $LiFePO_4$/C cathode material XRD refinement plots; and initial charge/discharge curves prepared into $LiFePO_4$/C at different multiplicity conditions at pH 1.0 and 2.5 (PDF)

■ AUTHOR INFORMATION

Corresponding Author

Xiaoting Hong − *Department of Chemistry, Zhejiang Sci-Tech University, Hangzhou 310018, China;* ● orcid.org/0000-

0002-2420-4257; Phone: +86 (0571) 86843228;
Email: hanren.xiaoting@gmail.com

Authors

Jiawu Peng − *Department of Chemistry, Zhejiang Sci-Tech University, Hangzhou 310018, China*

Qiongxiang Zhou − *Department of Chemistry, Zhejiang Sci-Tech University, Hangzhou 310018, China*

Kwan San Hui − *Engineering, Faculty of Science, University of East Anglia, Norwich NR4 7TJ, U.K.;* orcid.org/0000-0001-7089-7587

Bin Chen − *Zhejiang Agriculture and Forestry University, Lin'an 311300, China*

Complete contact information is available at:
https://pubs.acs.org/10.1021/acsomega.2c07838

Notes

The authors declare no competing financial interest.

■ REFERENCES

(1) Chen, S. P.; Lv, D.; Chen, J.; Zhang, Y.-H.; Shi, F.-N. Review on Defects and Modification Methods of LiFePO$_4$ Cathode Material for Lithium-Ion Batteries. *Energy Fuels* **2022**, *36*, 1232−1251.

(2) Goodenough, J. B.; Park, K.-S. The Li-Ion Rechargeable Battery: A Perspective. *J. Am. Chem. Soc.* **2013**, *135*, 1167−1176.

(3) Li, L.; Wu, L.; Wu, F.; Song, S.; Zhang, X.; Fu, C.; Yuan, D.; Xiang, Y. Review-Recent Research Progress in Surface Modification of LiFePO$_4$Cathode Materials. *J. Electrochem. Soc.* **2017**, *164*, A2138−A2150.

(4) Chung, S. Y.; Bloking, J. T.; Chiang, Y. M. Electronically conductive phospho-olivines as lithium storage electrodes. *Nat. Mater.* **2002**, *1*, 123−128.

(5) Massé, R. C.; Uchaker, E.; Cao, G. Beyond Li-ion: electrode materials for sodium- and magnesium-ion batteries. *Sci. China Mater.* **2015**, *58*, 715−766.

(6) Zhang, M.; Shi, Z.; Zhang, J.; Zhang, K.; Lei, L.; Dastan, D.; Dong, B. Greatly enhanced dielectric charge storage capabilities of layered polymer composites incorporated with low loading fractions of ultrathin amorphous iron phosphate nanosheets. *J. Mater. Chem. C* **2021**, *9*, 10414−10424.

(7) Shen, C.; Li, G.; Liu, L.; Li, P.; Xu, H.; Hu, H.; Wang, L. Facile fabrication of compact LiFePO$_4$/C composite with excellent atomically-efficient for high-energy-density Li-ion batteries. *J. Power Sources* **2021**, *496*, No. 229759.

(8) Xiao, P.; Henkelman, G. Kinetic Monte Carlo Study of Li Intercalation in LiFePO$_4$. *ACS Nano* **2018**, *12*, 844−851.

(9) Guo, J.; Mo, X.; Wu, F.; Yu, M. A novel environment-friendly synthesis of high purity micron iron phosphate and its application as a precursor of lithium iron phosphate. *Mater. Res. Express* **2020**, *7*, No. 095504.

(10) Chen, X.; Zhou, S.; Feng, C. Synthesis and electrochemical properties of calcium cobaltate as novel anode material. *J. Mater. Sci.: Mater. Electron.* **2020**, *31*, 16020−16026.

(11) Alam, S.; Iqbal, M. Z. Nickel-manganese phosphate: An efficient battery-grade electrode for supercapattery devices. *Ceram. Int.* **2021**, *47*, 11220−11230.

(12) Jiang, D.; Zhang, X.; Zhao, T.; Liu, B.; Yang, R.; Zhang, H.; Fan, T.; Wang, F. An improved synthesis of iron phosphate as a precursor to synthesize lithium iron phosphate. *Bull. Mater. Sci.* **2020**, *43*, No. 50.

(13) Liu, H.; Strobridge, F. C.; Borkiewicz, O. J.; Wiaderek, K. M.; Chapman, K. W.; Chupas, P. J.; Grey, C. P. Capturing metastable structures during high-rate cycling of LiFePO(4) nanoparticle electrodes. *Science* **2014**, *344*, No. 1252817.

(14) Orikasa, Y.; Maeda, T.; Koyama, Y.; Murayama, H.; Fukuda, K.; Tanida, H.; Arai, H.; Matsubara, E.; Uchimoto, Y.; Ogumi, Z. Transient Phase Change in Two Phase Reaction between LiFePO$_4$ and FePO$_4$ under Battery Operation. *Chem. Mater.* **2013**, *25*, 1032−1039.

(15) Sun, S.; An, Q.; Tian, Z.; Zhao, X.; Shen, X. Low-Temperature Synthesis of LiFePO$_4$ Nanoplates/C Composite for Lithium Ion Batteries. *Energy Fuels* **2020**, *34*, 11597−11605.

(16) Arinawati, M.; Hutama, A. P.; Yudha, C. S.; Rahmawati, M.; Purwanto, A. Facile rheological route method for LiFePO$_4$/C cathode material production. *Open Eng.* **2021**, *11*, 669−676.

(17) Ren, X.; Li, Z.; Cao, J.; Tian, S.; Zhang, K.; Guo, J.; Wen, L.; Liang, G. Enhanced rate performance of the mortar-like LiFePO$_4$/C composites combined with the evenly coated of carbon aerogel. *J. Alloys Compd.* **2021**, *867*, No. 158776.

(18) Eftekhari, A. Lithium-Ion Batteries with High Rate Capabilities. *ACS Sustainable Chem. Eng.* **2017**, *5*, 2799−2816.

(19) Deng, S.; Wang, H.; Liu, H.; Liu, J.; Yan, H. Research Progress in Improving the Rate Performance of LiFePO$_4$ Cathode Materials. *Nano-Micro Lett.* **2014**, *6*, 209−226.

(20) Wang, J. J.; Sun, X. L. Olivine LiFePO4: the remaining challenges for future energy storage. *Energy Environ. Sci.* **2015**, *8*, 1110−1138.

(21) Wang, Z.; Lu, Y. Facile Construction of High-Performance Amorphous FePO$_4$/Carbon Nanomaterials as Cathodes of Lithium-Ion Batteries. *ACS Appl. Mater. Interfaces* **2019**, *11*, 13225−13233.

(22) Zhang, T.; Lin, S.; Yu, J. Influence Mechanism of Precursor Crystallinity on Electrochemical Performance of LiFePO$_4$/C Cathode Material. *Ind. Eng. Chem. Res.* **2022**, *61*, 5181−5190.

(23) Latif, C.; Firdausi, A.; Nihlatunnur, N.; Saiyasombat, C.; Klysubun, W.; Subhan, A.; Zainuri, M.; Pratapa, S. Synchrotron crystal and local structures, microstructure, and electrical characterization of Cu-doped LiFePO$_4$/C via dissolution method with ironstone as Fe source. *J. Mater. Sci.: Mater. Electron.* **2022**, *33*, 17722−17732.

(24) Fischer, M. G.; Hua, X.; Wilts, B. D.; Castillo-Martinez, E.; Steiner, U. Polymer-Templated LiFePO$_4$/C Nanonetworks as High-Performance Cathode Materials for Lithium-Ion Batteries. *ACS Appl. Mater. Interfaces* **2018**, *10*, 1646−1653.

(25) Yan, C.; Wu, K.; Jing, P.; Luo, H.; Zhang, Y. Mg-doped porous spherical LiFePO$_4$/C with high tap-density and enhanced electrochemical performance. *Mater. Chem. Phys.* **2022**, *280*, No. 125711.

(26) Seher, J.; Fröba, M. Shape Matters: The Effect of Particle Morphology on the Fast-Charging Performance of LiFePO$_4$/C Nanoparticle Composite Electrodes. *ACS Omega* **2021**, *6*, 24062−24069.

(27) Zhu, Q.; Wang, X.; Miller, J. D. Advanced Nanoclay-Based Nanocomposite Solid Polymer Electrolyte for Lithium Iron Phosphate Batteries. *ACS Appl. Mater. Interfaces* **2019**, *11*, 8954−8960.

(28) Sun, C.; Rajasekhara, S.; Goodenough, J. B.; Zhou, F. Monodisperse Porous LiFePO$_4$ Microspheres for a High Power Li-Ion Battery Cathode. *J. Am. Chem. Soc.* **2011**, *133*, 2132−2135.

(29) Han, D.-W.; Ryu, W.-H.; Kim, W.-K.; Lim, S.-J.; Kim, Y.-I.; Eom, J.-Y.; Kwon, H.-S. Tailoring Crystal Structure and Morphology of LiFePO$_4$/C Cathode Materials Synthesized by Heterogeneous Growth on Nanostructured LiFePO$_4$ Seed Crystals. *ACS Appl. Mater. Interfaces* **2013**, *5*, 1342−1347.

(30) Lin, M.; Chen, Y.; Chen, B.; Wu, X.; Kam, K.; Lu, W.; Chan, H. L. W.; Yuan, J. Morphology-Controlled Synthesis of Self-Assembled LiFePO4/C/RGO for High-Performance Li-Ion Batteries. *ACS Appl. Mater. Interfaces* **2014**, *6*, 17556−17563.

(31) Wang, M.; Xue, Y.; Zhang, K.; Zhang, Y. Synthesis of FePO$_4$·2H$_2$O nanoplates and their usage for fabricating superior high-rate performance LiFePO$_4$. *Electrochim. Acta* **2011**, *56*, 4294−4298.

(32) Cao, F.; Li, D. Biotemplate synthesis of monodispersed iron phosphate hollow microspheres. *Bioinspiration Biomimetics* **2010**, *5*, No. 016005.

(33) Pramanik, M.; Imura, M.; Lin, J.; Kim, J.; Kim, J. H.; Yamauchi, Y. Shape-controlled synthesis of mesoporous iron phosphate materials with crystallized frameworks. *Chem. Commun.* **2015**, *51*, 13806−13809.

(34) Guo, J.; Yu, M.; Wu, F. Preparation of high purity iron phosphate based on the advanced liquid-phase precipitation method and its enhanced properties. *J. Solid State Chem.* **2020**, *287*, No. 121346.

(35) Mo, R.; Li, F.; Tan, X.; Xu, P.; Tao, R.; Shen, G.; Lu, X.; Liu, F.; Shen, L.; Xu, B.; et al. High-quality mesoporous graphene particles as high-energy and fast-charging anodes for lithium-ion batteries. *Nat. Commun.* **2019**, *10*, No. 1474.

(36) Duan, S.-Y.; Piao, J.-Y.; Zhang, T.-Q.; Sun, Y.-G.; Liu, X.-C.; Cao, A.-M.; Wan, L.-J. Kinetically controlled formation of uniform FePO4 shells and their potential for use in high-performance sodium ion batteries. *NPG Asia Mater.* **2017**, *9*, No. e414.

(37) Qian, L.; Xia, Y.; Zhang, W.; Huang, H.; Gan, Y.; Zeng, H.; Tao, X. Electrochemical synthesis of mesoporous $FePO_4$ nanoparticles for fabricating high performance $LiFePO_4/C$ cathode materials. *Microporous Mesoporous Mater.* **2012**, *152*, 128−133.

(38) Song, Y.; Zavalij, P. Y.; Suzuki, M.; Whittingham, M. S. New Iron(III) Phosphate Phases: Crystal Structure and Electrochemical and Magnetic Properties. *Inorg. Chem.* **2002**, *41*, 5778−5786.

(39) Nagaraju, P.; Srilakshmi, C.; Pasha, N.; Lingaiah, N.; Suryanarayana, I.; Prasad, P. S. S. Effect of P/Fe ratio on the structure and ammoxidation functionality of Fe-P-O catalysts. *Appl. Catal., A* **2008**, *334*, 10−19.

(40) Yang, F.; Zhang, H.; Shao, Y.; Song, H.; Liao, S.; Ren, J. Formic acid as additive for the preparation of high-performance FePO4 materials by spray drying method. *Ceram. Int.* **2017**, *43*, 16652−16658.

(41) Li, S.; Liu, X.; Mi, R.; Liu, H.; Li, Y.; Lau, W. M.; Mei, J. A facile route to modify ferrous phosphate and its use as an iron-containing resource for LiFePO4 via a polyol process. *ACS Appl. Mater. Interfaces* **2014**, *6*, 9449−9457.

(42) Dhaybi, S.; Marsan, B.; Hammami, A. A novel low-cost and simple colloidal route for preparing high-performance carbon-coated LiFePO4 for lithium batteries. *J. Energy Storage* **2018**, *18*, 259−265.

(43) Xi, Y.; Lu, Y. Toward Uniform In Situ Carbon Coating on Nano-LiFePO4 via a Solid-State Reaction. *Ind. Eng. Chem. Res.* **2020**, *59*, 13549−13555.

(44) Cui, Q.; Luo, C.; Li, G.; Wang, G.; Yan, K. Environmentally Friendly Synthesis of LiFePO4 Using Fe−P Waste Slag and Greenhouse Gas CO_2. *Ind. Eng. Chem. Res.* **2016**, *55*, 7069−7075.

(45) Wang, Z.; Lu, Y. Amorphous FePO4/Carbon Nanotube Cathode Preparation via in Situ Nanoprecipitation and Coagulation in a Microreactor. *ACS Omega* **2019**, *4*, 14790−14799.

(46) Abdelhak, J.; Cherni, S. N.; Zid, M. F.; Driss, A. Crystal structure, spectroscopic and magnetic properties of a new iron(III) complex. *J. Struct. Chem.* **2015**, *56*, 654−661.

(47) Khan, S.; Raj, R. P.; George, L.; Kannangara, G. S. K.; Milev, A.; Varadaraju, U. V.; Selvam, P. Surfactant-Mediated and Morphology-Controlled Nanostructured LiFePO(4)/Carbon Composite as a Promising Cathode Material for Li-Ion Batteries. *ChemistryOpen* **2020**, *9*, 23−31.

(48) De Tommaso, G.; Iuliano, M. Acid−Base Properties of the Surface of Hydrous Ferric Phosphate in Aqueous Solutions. *J. Chem. Eng. Data* **2012**, *57*, 52−59.

(49) Guan, H.; Xu, C.; Sheng, Y.; Song, Y.; Zheng, K.; Shi, Z.; Zou, H. Controlling the Morphology and Size of $GdF_3:RE^{3+}$ (RE = Dy, Tb, and Sm) by pH Value: Growth Mechanism, Energy Transfer, and Luminescent Properties. *J. Phys. Chem. C* **2017**, *121*, 6884−6897.

(50) Zhang, Y.; Alarco, J. A.; Best, A. S.; Snook, G. A.; Talbot, P. C.; Nerkar, J. Y. Re-evaluation of experimental measurements for the validation of electronic band structure calculations for LiFePO4 and FePO4. *RSC Adv.* **2019**, *9*, 1134−1146.

(51) Song, Y.; Xie, B.; Song, S.; Lei, S.; Sun, W.; Xu, R.; Yang, Y. Regeneration of LiFePO4 from spent lithium-ion batteries via a facile process featuring acid leaching and hydrothermal synthesis. *Green Chem.* **2021**, *23*, 3963−3971.

(52) Kobayashi, S.; Fisher, C. A.; Kato, T.; Ukyo, Y.; Hirayama, T.; Ikuhara, Y. Atomic-Scale Observations of (010) LiFePO4 Surfaces Before and After Chemical Delithiation. *Nano Lett.* **2016**, *16*, 5409−5414.

(53) Jarolimek, K.; Risko, C. Modification of the LiFePO4 (010) Surface Due to Exposure to Atmospheric Gases. *ACS Appl. Mater. Interfaces* **2021**, *13*, 29034−29040.

(54) Khan, S.; Raj, R. P.; Mohan, T. V. R.; Bhuvaneswari, S.; Varadaraju, U. V.; Selvam, P. Electrochemical performance of nano-LiFePO4 embedded ordered mesoporous nitrogenous carbon composite as cathode material for Li-ion battery applications. *J. Electroanal. Chem.* **2019**, *848*, No. 113242.

(55) Khan, S.; Raj, R. P.; Rama Mohan, T. V.; Selvam, P. Electrochemical performance of nano-sized LiFePO(4)-embedded 3D-cubic ordered mesoporous carbon and nitrogenous carbon composites. *RSC Adv.* **2020**, *10*, 30406−30414.

(56) Zhang, J.; Nie, N.; Liu, Y.; Wang, J.; Yu, F.; Gu, J.; Li, W. Boron and Nitrogen Codoped Carbon Layers of LiFePO4 Improve the High-Rate Electrochemical Performance for Lithium Ion Batteries. *ACS Appl. Mater. Interfaces* **2015**, *7*, 20134−20143.

(57) Tian, H.; Zhao, X.; Zhang, J.; Li, M.; Lu, H. LiFePO4 Anchored on Pristine Graphene for Ultrafast Lithium Battery. *ACS Appl. Energy Mater.* **2018**, *1*, 3497−3504.

(58) Kim, J.-K.; Kim, D.-S.; Lim, D.-H.; Matic, A.; Chauhan, G. S.; Ahn, J.-H. Effect of carbon coating methods on structural characteristics and electrochemical properties of carbon-coated lithium iron phosphate. *Solid State Ionics* **2014**, *262*, 25−29.

(59) Wang, J.; Sun, X. Understanding and recent development of carbon coating on LiFePO4 cathode materials for lithium-ion batteries. *Energy Environ. Sci.* **2012**, *5*, 5163−5185.

⬚ Recommended by ACS